

Lithospheric Structure underneath the Archean Tanzania Craton and Adjacent Regions from a Joint Inversion of Receiver Functions and Rayleigh-Wave Phase Velocity Dispersion

Tuo Wang^{1,2} , Stephen S. Gao² , Qiuyue Yang² , Ling Chen¹ , and Kelly H. Liu^{*2} 

Abstract

Lithospheric structure beneath the Archean Tanzania craton and adjacent regions, including segments of the East African rift system (EARS) and the Proterozoic–early Paleozoic orogenic belts between the EARS and the craton, is imaged by a joint inversion of receiver functions and Rayleigh wave dispersion measurements derived from ambient seismic noise for shorter periods and teleseismic data for longer periods. Our resulting crustal thickness, crustal V_p/V_s measurements and 3D shear-wave velocity model for the upper 120 km show a clear spatial correspondence with major surficial geological features. The new results suggest the presence of a mafic layer in the bottom of the crust of the entire Archean craton, which is previously only identified beneath the southern portion of the craton. High crustal V_p/V_s values measured in the Rungwe Volcanic Province and most areas of the Kenya and Tanganyika rift segments can be attributed to a combined result of basaltic sediments atop the crust, magmatic intrusion, and crustal partial melting. The Kivu Volcanic Province and parts of the Kenya rift segment are characterized by localized lower-than-normal crustal V_p/V_s values and shear velocities in the lower crust and uppermost mantle, which, given the presence of large volume of CO_2 from surficial observations, can be best interpreted by CO_2 -filled fractures or conduits. Lower-than-normal shear velocities in the uppermost mantle are revealed beneath almost the entire study region with the lowest values found in all the three volcanic provinces. The low velocities are indicative of an underplated layer formed by mantle-derived magmatic materials trapped below the Moho. The relatively low velocities beneath the volcanic provinces might be caused by a higher degree of partial melting in the uppermost mantle.

Cite this article as Wang, T., S. S. Gao, Q. Yang, L. Chen, and K. H. Liu (2022). Lithospheric Structure underneath the Archean Tanzania Craton and Adjacent Regions from a Joint Inversion of Receiver Functions and Rayleigh-Wave Phase Velocity Dispersion, *Seismol. Res. Lett.* **XX**, 1–15, doi: [10.1785/0220210296](https://doi.org/10.1785/0220210296).

Introduction

Situated in the central area of East Africa, the Tanzania craton (TC) is nestled between the western and eastern branches of the East African rift system (EARS). A number of Proterozoic–early Paleozoic orogenic belts, including the Ruwenzori, Karagwe–Ankole, Ubendian, Usagaran, and the Mozambique belts, lie between the TC and the two branches (Fig. 1). The Archean craton (~2.5 Ga) mainly consists of granites, gneisses, and amphibolites, with some greenstone belts in its northern portion (Cahen *et al.*, 1984; Last *et al.*, 1997). Embedded in the center of the high-elevation East African plateau, the TC is characterized by a mean elevation of ~1260 m (Nyblade and Robinson, 1994; Weeraratne *et al.*, 2003), and the onset time of the uplift has been suggested to be ~40 Ma (Smith, 1994; Spiegel *et al.*, 2007).

The western branch mainly contains the Tanganyika rift segment (TRS) and Malawi rift segment (MRS) and accommodates several isolated volcanic provinces, including the Virunga, Kivu, and Rungwe volcanic provinces (Fig. 1). The TRS is bordered by several northwest-trending, 80–100-km-long normal faults, creating broad asymmetric rift basins with fluviolacustrine sediments reaching up to 7 km in thickness (Morley, 1988).

1. State Key Laboratory of Lithospheric Evolution, Institute of Geology and Geophysics, Chinese Academy of Sciences, Beijing, China,  <https://orcid.org/0000-0001-7492-8985> (TW);  <https://orcid.org/0000-0001-7170-5954> (LC); 2. Geology and Geophysics Program, Missouri University of Science and Technology, Rolla, Missouri, U.S.A.,  <https://orcid.org/0000-0001-7530-7128> (SSG);  <https://orcid.org/0000-0002-6667-365X> (QY);  <https://orcid.org/0000-0001-7691-9556> (KHL)

*Corresponding author: liukh@mst.edu

© Seismological Society of America

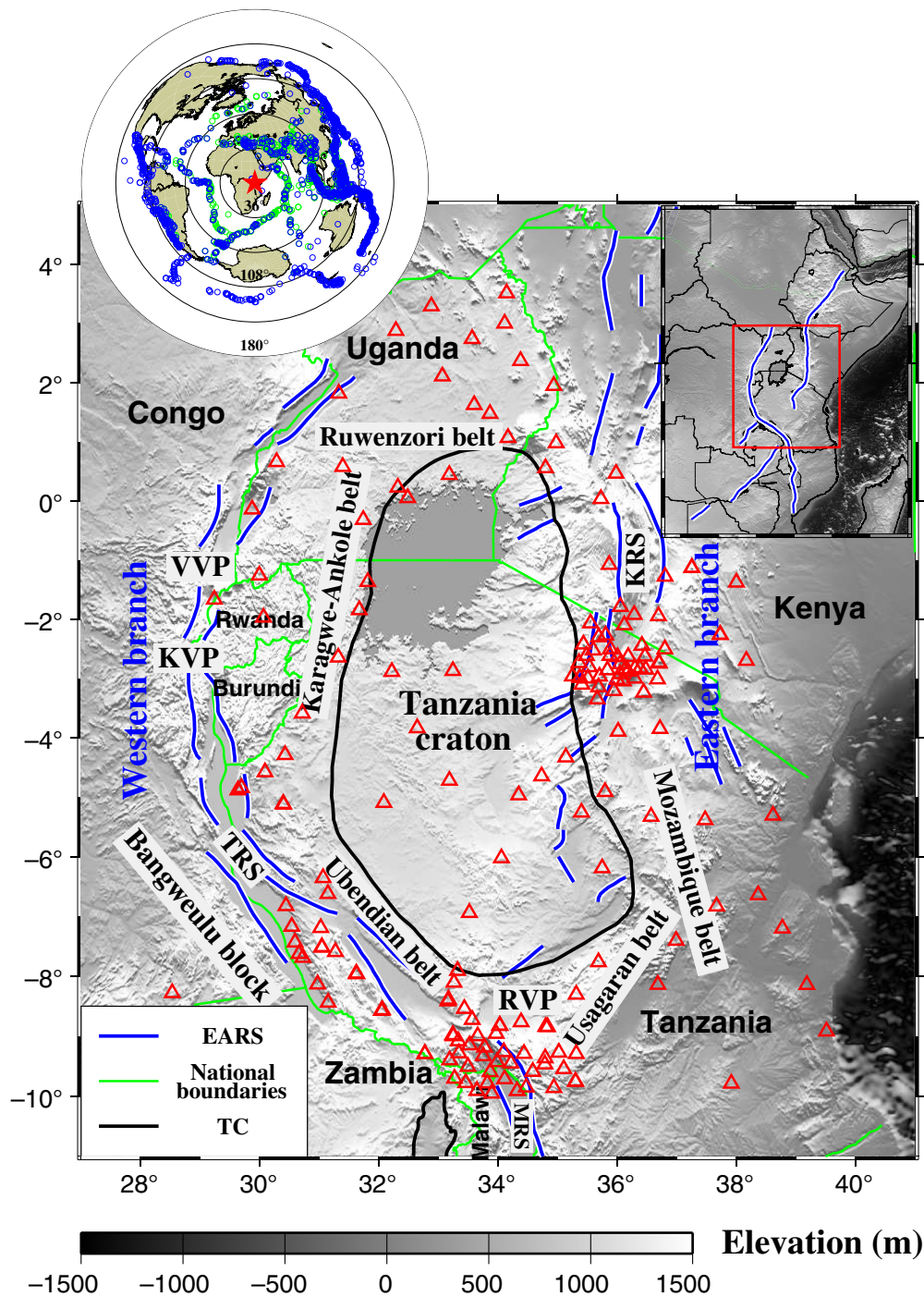


Figure 1. Topographic map showing the distribution of the seismic stations used in the study (open triangles) and major tectonic setting of the study area. The red pentagram in the azimuthal equidistant projection map in the upper left corner indicates the center of the study area. The blue open circles in the projection map represent the earthquakes used for receiver function (RF) analysis, whereas the green open circles are for the teleseismic two-station (TS) surface-wave dispersion analysis. The inset in the upper right corner shows the topography of East Africa, the location of the East African Rift System (blue curves), and the study region (open red rectangle). EARS, East African rift system; KRS, Kenya rift segment; KVP, Kivu Volcanic Province; MRS, Malawi rift segment; RVP, Rungwe Volcanic Province; TC, Tanzania craton; TRS, Tanganyika rift segment; VVP, Virunga Volcanic Province. The color version of this figure is available only in the electronic edition.

Initiated at ~25 Ma, the north-south-oriented MRS is one of the youngest rift segments of the western branch (Roberts *et al.*, 2012). Volcanisms in the western branch date back to ~12 Ma in the Virunga Volcanic Province, ~8 Ma in the Kivu Volcanic Province, and ~25 Ma in the Rungwe Volcanic Province (Ebinger *et al.*, 1989; Kampunzu *et al.*, 1998; Roberts *et al.*, 2012). The Kenya rift segment (KRS), developed along the northeastern margin of the TC, is the southernmost portion of the volcanically active eastern branch. Rifting-related volcanism progressively migrated southward along this branch, starting at ~30 Ma in northern Kenya to ~12 Ma in southern Kenya (George *et al.*, 1998).

A shear velocity model constructed by Julia *et al.* (2005) manifests an approximately 2–4-km-thick mafic layer at the bottom of the crust underneath the southern TC, which might be formed by mafic rock emplacement during a number of magmatic events (Halls *et al.*, 1987). Because of the limitation of data coverage, the lower crustal velocity structure of the northern TC has not been adequately investigated. Low crustal velocities are observed beneath the southern terminus of the KRS (Plasman *et al.*, 2017), when combined with their relatively thin crust and high V_p/V_s measurements beneath the rift axis, a crustal partial melting model, which might be associated with the rift extension, has been proposed (Plasman *et al.*, 2017). Low crustal velocities caused by rifting are also found in the MRS and Rungwe Volcanic Province to the northwest of

the MRS (Accardo *et al.*, 2017, 2020). In contrast to the high V_P/V_S values found beneath the rift axis of the KRS (Plasman *et al.*, 2017), the two boundaries of the southern KRS are characterized by lower-than-normal V_P/V_S values, which are attributed to gaseous CO₂ associated with volcanic plumbing probably originated from the lower crust and/or upper mantle (Plasman *et al.*, 2017; Roecker *et al.*, 2017), a hypothesis that is consistent with surficial observations of the existence of CO₂ in the vicinity of the area (Lee *et al.*, 2016). As detailed subsequently, our resulting crustal structure from the H - V_P/V_S receiver function (RF) stacking analysis suggests that crustal partial melting is also needed to interpret the observed high- V_P/V_S values beneath these regions. Even for the TRS, which is widely accepted as an amagmatic extension model (O'Donnell *et al.*, 2016), a certain percentage of crustal partial melting is required.

The uplifting mechanism of the East African plateau has long been debated. Last *et al.* (1997) measure the crustal thickness (H) values of the TC and calculate the thickness of the Archean crust prior to the uplift under the assumption of the Airy's isostatic theory. The calculated H values of the TC before it was elevated (~22 km) are much smaller than the global average value for Precambrian terrains (Last *et al.*, 1997), and thus they suggest that the high elevation of the East African plateau is not caused by crustal thickening but might be associated with low densities in the mantle. The conclusions are supported by other seismological studies that report generally consistent H measurements (e.g., Dugda *et al.*, 2005; Tugume *et al.*, 2012). Widespread low seismic velocities in the uppermost mantle beneath the study region have been revealed (Green *et al.*, 1991; Achauer and The KRISP Teleseismic Working Group, 1994; Fishwick, 2010; Hansen *et al.*, 2012; Accardo *et al.*, 2020). A low velocity anomaly beneath the TC extending from ~140 to 350 km deep is interpreted as an upper mantle plume, and dynamic support of the plume is proposed to be responsible for the uplift of the East African Plateau by providing the required buoyancy (Weeraratne *et al.*, 2003). The origin of the plume is speculated to be in the lower mantle on the basis of seismic tomography (Hansen *et al.*, 2012; Mulibo and Nyblade, 2013a; Tsekhmistrenko *et al.*, 2021), RF (Mulibo and Nyblade, 2013b), and seismic anisotropy (Bagley and Nyblade, 2013) studies. In contrast, the lower mantle plume model is in disagreement with observations from a more recent RF analysis, which suggests that the thickness of the mantle transition zone is ~252 km beneath the TC, a value that is comparable to the global average of ~250 km and thus is indicative of the present-day absence of a thermal upwelling beneath the TC originating from the lower mantle (Sun *et al.*, 2017).

In this study, a nonlinear Bayesian Monte Carlo joint inversion of RFs and Rayleigh-wave phase velocity dispersion is utilized to produce a high-resolution 3D shear-wave velocity model for the upper 120 km beneath the TC and adjacent areas. The H - V_P/V_S RF stacking analysis (Zhu and

Kanamori, 2000) is applied to obtain crustal structures beneath the study region and to provide constraints for better determining the Moho depth for the joint inversion. Rayleigh-wave phase velocity dispersion measurements are extracted from ambient noise data at short periods (6–24 s) to improve the inversion resolution by utilizing higher frequency surface waves (Ritzwoller *et al.*, 2002; Shapiro and Campillo, 2004) and from teleseismic data at longer periods (28–80 s). By taking advantages from RF and surface-wave dispersion, the inverted shear velocity model provides additional constraints and new insights into the lithospheric structure and evolution of the Archean craton and Cenozoic rift segments.

Data and Methods

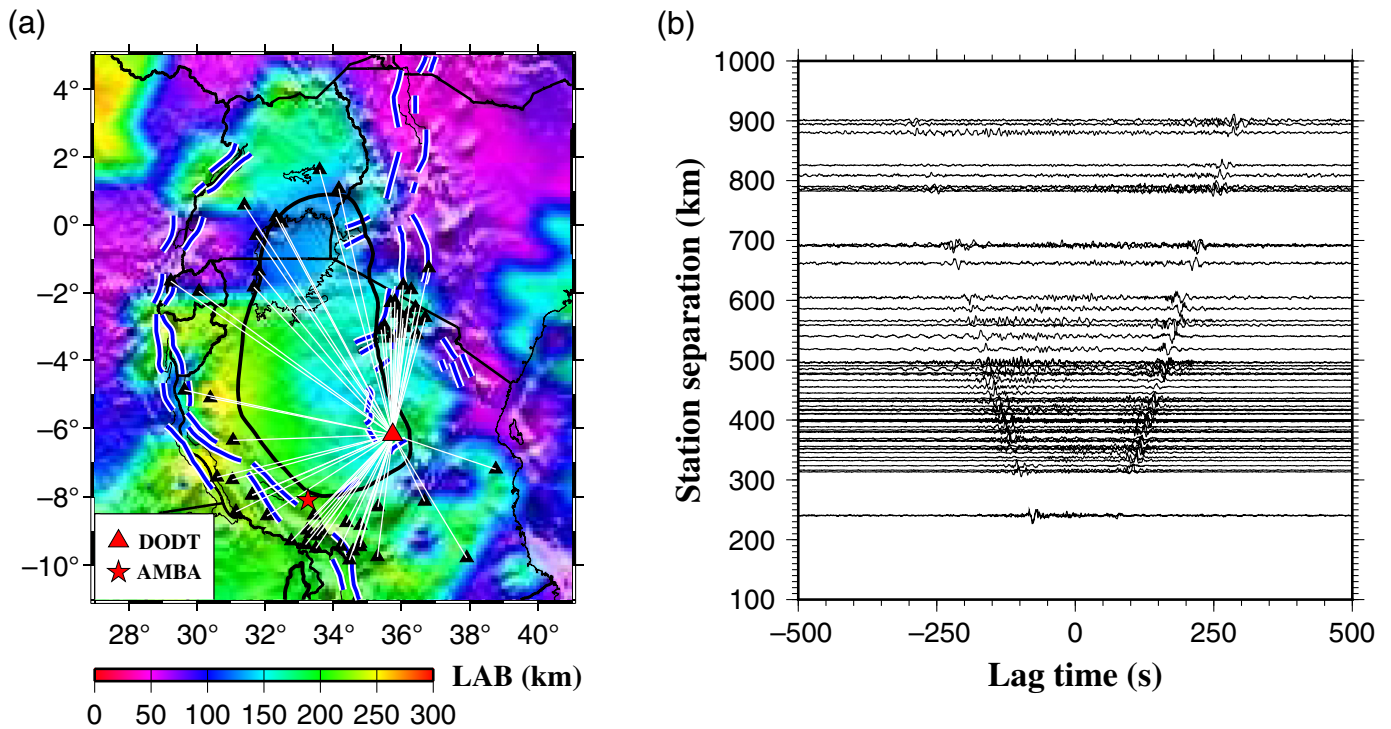
Data

All the broadband seismic data used in the study were requested from the Incorporated Research Institutions for Seismology Data Management Center (IRIS-DMC). The data were recorded by 180 stations between May 1994 and December 2018 with variable durations of recording, within the area of 28° E–40° E, and 10° S–4° N (Fig. 1). To obtain Rayleigh-wave phase velocity measurements from ambient noise, we requested vertical-component broadband waveforms with one-day length (86,400 s) from the IRIS-DMC, and uniformly resampled the seismograms to 5 Hz for cross-correlation processing. For extracting Rayleigh-wave phase velocity measurements from teleseismic events, broadband seismic data in the epicentral distance range of 10°–130° were requested from 1996 earthquakes ($M_b \geq 5.7$) (Fig. 1), and the seismograms were then uniformly resampled to 1 Hz.

For computing RFs, data were requested from 1310 teleseismic events in the epicentral distance range of 30°–100° from the IRIS-DMC. We used an empirical formula to calculate the cutoff magnitude (M_c) that balances the quantity and quality of the requested data, that is, $M_c = 5.2 + (\Delta - \Delta_{\min}) / (180 - \Delta_{\min}) - D/D_{\max}$, in which Δ represents the epicentral distance in degrees and D represents the focal depth in kilometers, $\Delta_{\min} = 30^\circ$ and $D_{\max} = 700$ km (Liu and Gao, 2010). Finally, 5107 high-quality three-component seismograms met the previous criteria of epicentral distance range and M_c . The retained seismograms used to generate RFs are 60 s in length, starting from 5 s prior to and 55 s after the theoretically calculated first P -wave arrival according to the IASP91 velocity model (Kennett and Engdahl, 1991).

Methods

Short-period Rayleigh-wave data processing. Rayleigh-wave phase velocity dispersion at short periods (6–24 s) was extracted from ambient seismic noise data using the empirical Green's function (EGF) analysis with an interval of 2 s (Yao *et al.*, 2006). The procedure including five main steps closely follows those in Yao *et al.* (2006) and Wang *et al.* (2019) and is briefly introduced subsequently. First, data from every single



station were preprocessed by removing the mean, linear trend, and the instrumental response, and ambient seismic noise signals were obtained after applying a spectral whitening (Bensen *et al.*, 2007). Second, daily cross correlations were computed between each of the station pairs in the frequency domain to produce time series with positive and negative time coordinates (Fig. 2), and the two-sided time series were compressed to one-sided ones by averaging the positive and negative components and were stacked to enhance the signal-to-noise ratio (SNR) to obtain EGFs (Yao *et al.*, 2006; Bensen *et al.*, 2007). Third, using a modified far-field approximation and an image transformation technique (Yao *et al.*, 2005), Rayleigh-wave phase velocity dispersion curves were estimated from the EGFs. Three criteria, including (1) the SNR is larger than 5, (2) the distance between two stations is greater than three times the longest wavelength, and (3) the phase velocity dispersion measurements are in general agreement with global models (i.e., Shapiro and Ritzwoller, 2002), were applied to reject unreliable phase velocity dispersion curves estimated from the stacked EGFs (e.g., Wang *et al.*, 2019). Finally, using the inversion procedures in Yao *et al.* (2010) and Montagner (1986), 2D phase velocity maps at different periods were inverted from the 673 selected 1D phase velocity dispersion curves that were deemed as reliable.

Long-period Rayleigh-wave data processing. Long-period (28–80 s) dispersion measurements were extracted from teleseismic events using the teleseismic surface-wave two-station (TS) analysis with an interval of 4 s (Yao *et al.*, 2005). After single-station preprocessing, cross-correlation amplitude images

Figure 2. Cross-correlation results between station DODT (red triangle) and other stations (black triangles). (a) Ray paths (white lines) between station pairs. The background shows the variation of the lithosphere–asthenosphere boundary (LAB) depth (Pasyanos *et al.*, 2014). The red pentagram represents station AMBA mentioned in Figure 5. (b) 2–40 s band-pass filtered cross-correlation functions. The color version of this figure is available only in the electronic edition.

were obtained from station pairs and were transformed into phase velocity images using an image transformation technique (Yao *et al.*, 2005) for experience-based manual selection. A total of 1475 reliable measurements were retained after the manual selection. The selected Rayleigh-wave phase velocity dispersion curves were inverted to create phase velocity distributions at different periods using the same technique as that applied to the short-period ones. The grid dimension for all the periods for both the ambient noise and teleseismic events is $0.25^\circ \times 0.25^\circ$ with a sampling step of 0.05° . To obtain reliable phase velocities, only grids with at least one ray path were retained.

Horizontal checkerboard resolution test. A synthetic checkerboard resolution test was conducted to check the robustness of the inverted phase velocities from all periods (Fig. 3). The target model was synthesized with alternating positive and negative velocity anomaly values of 0.2 km/s and -0.2 km/s, respectively, representing a 5% perturbation relative to the reference value of 4 km/s, in $2.5^\circ \times 2.5^\circ$ grids with a sampling step of 0.25° (Fig. 3c). The same inversion procedures as those used for the observed data were applied on the

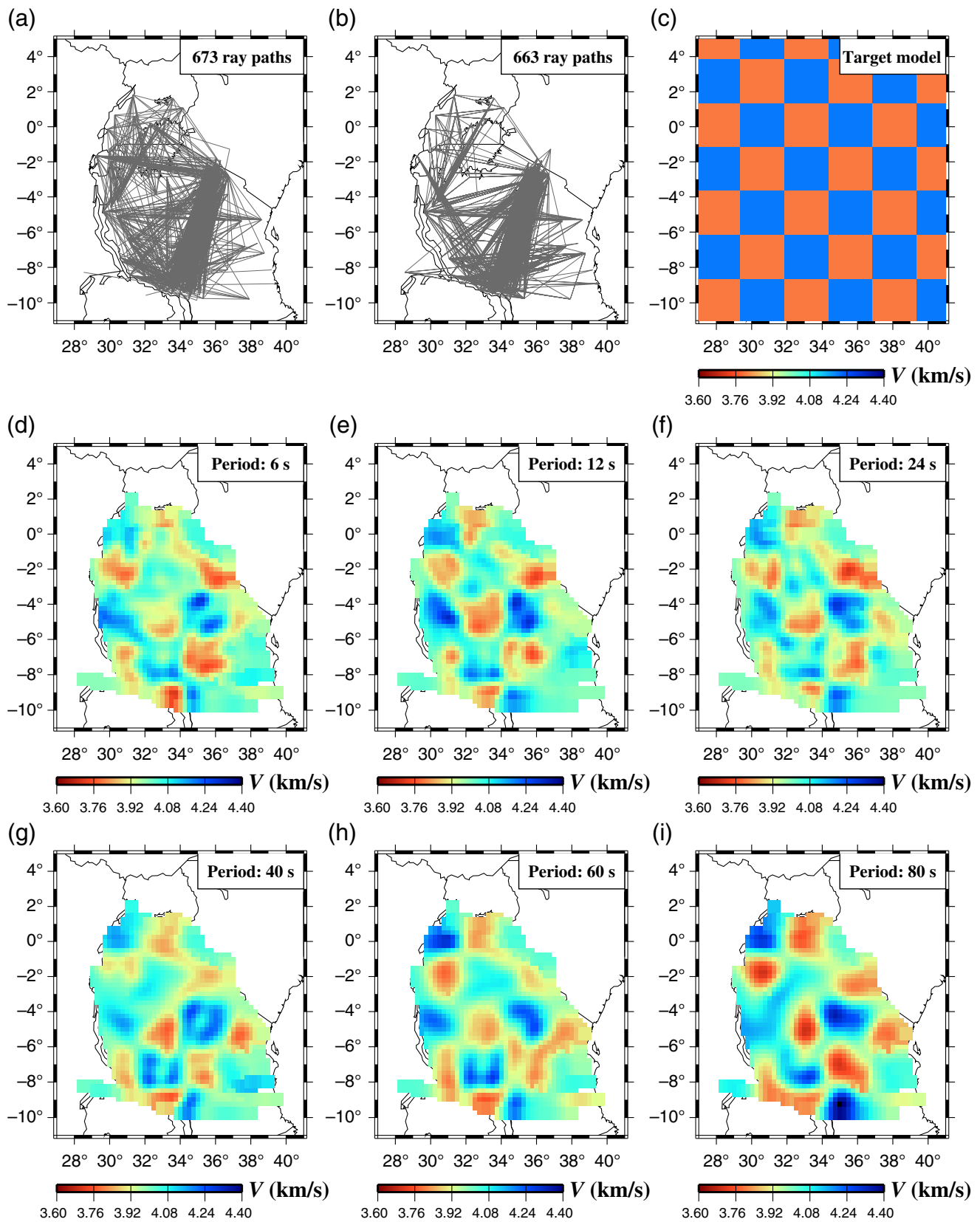


Figure 3. Ray-path coverages and results of checkerboard resolution test. (a) Ray paths for the empirical Green's function (EGF) analysis. Only the ones with reliable Rayleigh-wave phase velocity dispersion curves are plotted. (b) Ray paths for the teleseismic TS analysis. (c) Target checkerboard model. The color bar represents input values with alternating positive and negative 5%

perturbations of the reference value of 4 km/s. (d-f) Recoveries from the EGF analysis at the periods of 6, 12, and 24 s, respectively. (g-i) Recoveries from the teleseismic TS analysis for 40, 60, and 80 s, respectively. The color version of this figure is available only in the electronic edition.

synthetic model for generating the recovered results at different periods. Figure 3d–i displays the recoveries at the periods of 6, 12, 24, 40, 60, and 80 s. The reconstructed pattern of the checkerboards and the magnitude of anomalies are acceptable and indicate a reasonable resolution for most of the grids.

RF data processing. All original seismograms were filtered by a four-pole, two-pass band-pass Bessel filter in the frequency band between 0.06 and 1.2 Hz, and events with an SNR equal to or smaller than four were rejected for computing the RFs. The filtered seismograms were then converted into radial RFs by applying a procedure of frequency-domain water-level deconvolution (Clayton and Wiggins, 1976) with a water level value of 0.03 (e.g., Kong *et al.*, 2020). To determine the optimal H and V_p/V_S measurements beneath seismic stations, the H - V_p/V_S RF stacking procedure (Zhu and Kanamori, 2000) was used to search for the maximum stacking amplitude of the PmS , $PPmS$, and $PSmS$ phases (with weighting factors of 0.5, 0.3, and 0.2, respectively, e.g., Nair *et al.*, 2006). The reference velocity for stacking (V_p) is fixed to 6.1 km/s, which is a typical value for continental crust.

A 10-iterations bootstrap resampling approach (Efron and Tibshirani, 1986) was applied to compute the mean H and crustal V_p/V_S values and to estimate the corresponding standard deviations. A total of 5107 high-quality RFs recorded by 164 out of 180 seismic stations were selected. Stations close to each other (less than 1.0 km in distance) were combined together, and the combined station was named as the same as that recorded the greatest number of RFs. The number of station sites after the combination was reduced from 164 to 156. RFs from approximately 73.1% (114 out of 156) of the sites were found to lead to reliable H and crustal V_p/V_S measurements.

Joint inversion data processing. RFs are widely used to determine interfaces beneath the surface but are not ideal for providing seismic velocity information between the interfaces or away from the stations. Surface-wave dispersion carries velocity information along the ray paths of station pairs and between different interfaces but is not sensitive to velocity interfaces. Consequently, we jointly inverted the two data sets using a nonlinear Bayesian Monte Carlo algorithm (Shen *et al.*, 2013), which relies on repeated random sampling in a broad model space for data misfit under the constraint of the probability distribution of the model parameters based on the observed data.

For each station, the optimal H and crustal V_p/V_S values obtained from the RF analysis were used to construct a two-layer initial model with the top layer representing the crystalline crust and the bottom layer representing the uppermost mantle. Shear-wave velocities in the initial model from the surface to the Moho (top layer) were acquired by interpolating shear velocities in the IASP91 velocity model (Kennett and

Engdahl, 1991) using four B-spline coefficients. From the Moho to 120 km deep (bottom layer), the reference shear-wave velocities were obtained using five B-spline coefficients based on the IASP91 model. The prior distribution was determined by a random walk in the model space with two steps performed. The first step is to initiate the random point following the prior constraints proposed by Shen *et al.* (2013). If the random point could not meet the constraints, it would be rejected and replaced with a new one. The second step is to introduce a random jump, which allows all parameters to perturb simultaneously by randomly choosing new values governed by a Gaussian probability distribution adjacent to the previous ones. The Gaussian width for the nine B-spline coefficients and crustal thickness is set to be 0.05 km/s and 1.00 km, respectively (e.g., Shen *et al.*, 2013). If the produced model does not obey the prior constraints or exceeds the accepted perturbation magnitude, the model search would be reinitiated. The Monte Carlo sampling was initiated at 10 independent random models to avoid being affected by the starting points, and the number of iterations is 3000. Models were accepted when they meet the criterion by a combined root mean square misfit function for the joint inversion (Shen *et al.*, 2013).

Results

Rayleigh-wave phase velocities

At the period of 6 s (Fig. 4a), low phase velocities are observed in the Mozambique Belt, the central part of the TC, and the western and eastern branches of the EARS. Low velocities beneath the two branches may reflect the presence of loose sediments and water. Continuing downward to the periods of 12 and 24 s (Fig. 4b,c), low velocities persist in the two branches, and those beneath the Mozambique Belt gradually diminish. Starting from the period of 40 s (Fig. 4d–f), the central TC is dominated by high velocity anomalies, whereas the two EARS branches are characterized by low velocity anomalies.

Shear-wave velocity distribution

Shear-wave velocity curves from the surface to the depth of 120 km with an interval of 0.5 km were obtained from the joint inversion. Figure 5 shows examples of inversion results at two stations. Because for a given station, the initial inversion model only has one interface (the Moho discontinuity), the fitting to the stacked RF was attempted only for the time window containing the PmS phase. Subsequently, the 1D shear-wave velocity curves observed at all the stations were interpolated to obtain spatially continuous shear-wave velocity maps at different depths (Fig. 6).

At the depth of 6 km (Fig. 6a), low shear velocities relative to the IASP91 global model are observed beneath the three volcanic provinces, northern TRS, southern KRS, and the northern end of the MRS. The low shear velocities extend to the midcrust (16 km) and become more distinct

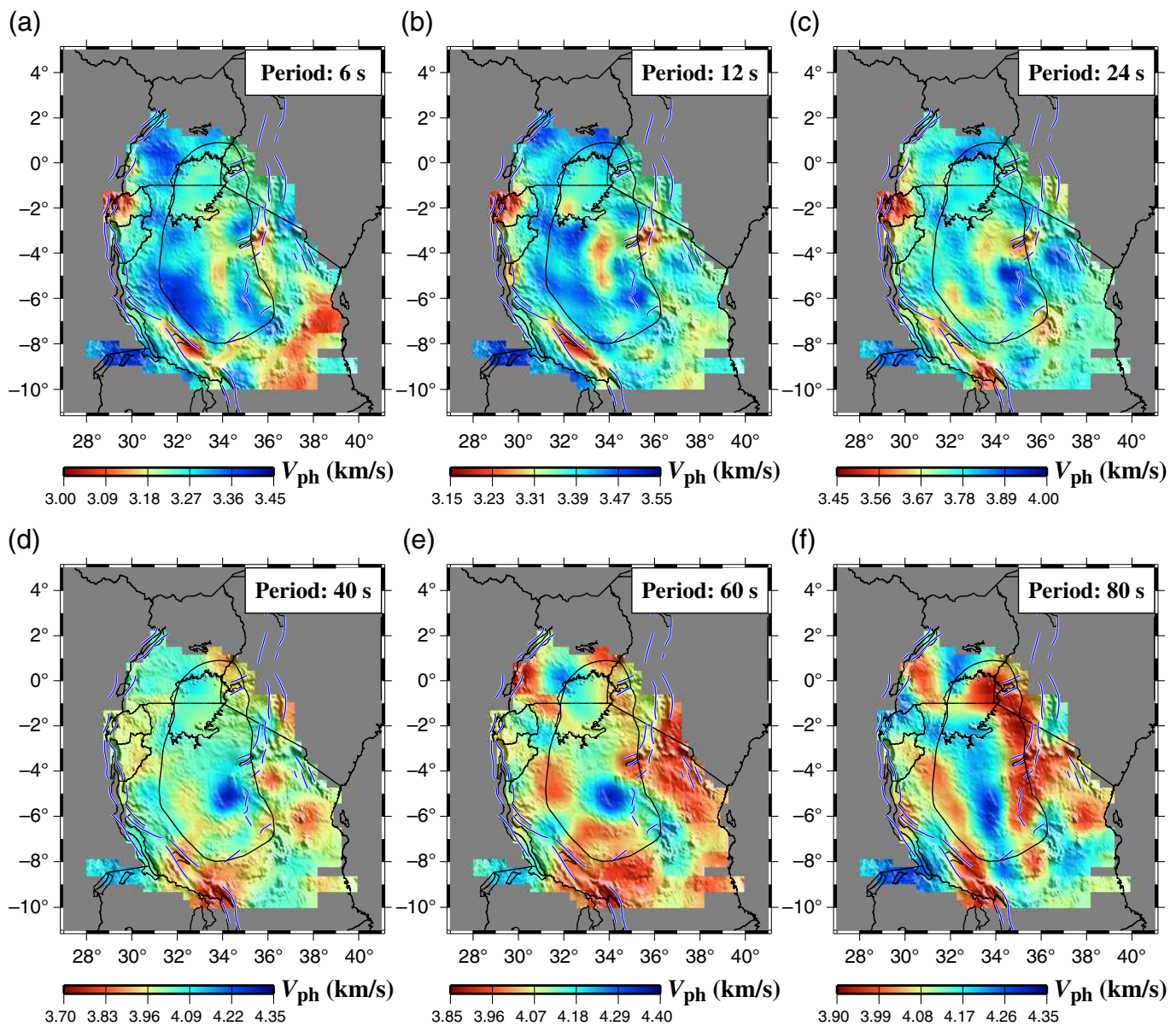


(Fig. 6b). At the depth of 30 km (Fig. 6c), the low velocities beneath the western branch observed at shallower depths turn to relatively higher velocities. From 60 to 120 km, the southern KRS, Mozambique Belt, and the northern tip of the MRS are characterized by low velocities, whereas the TC is characterized by high velocities (Fig. 6d–f). In most cases, the boundaries between the low and high velocities agree well with the boundaries of tectonic provinces observed at the surface, especially for the southeastern portion of the study area (e.g., Fig. 6f).

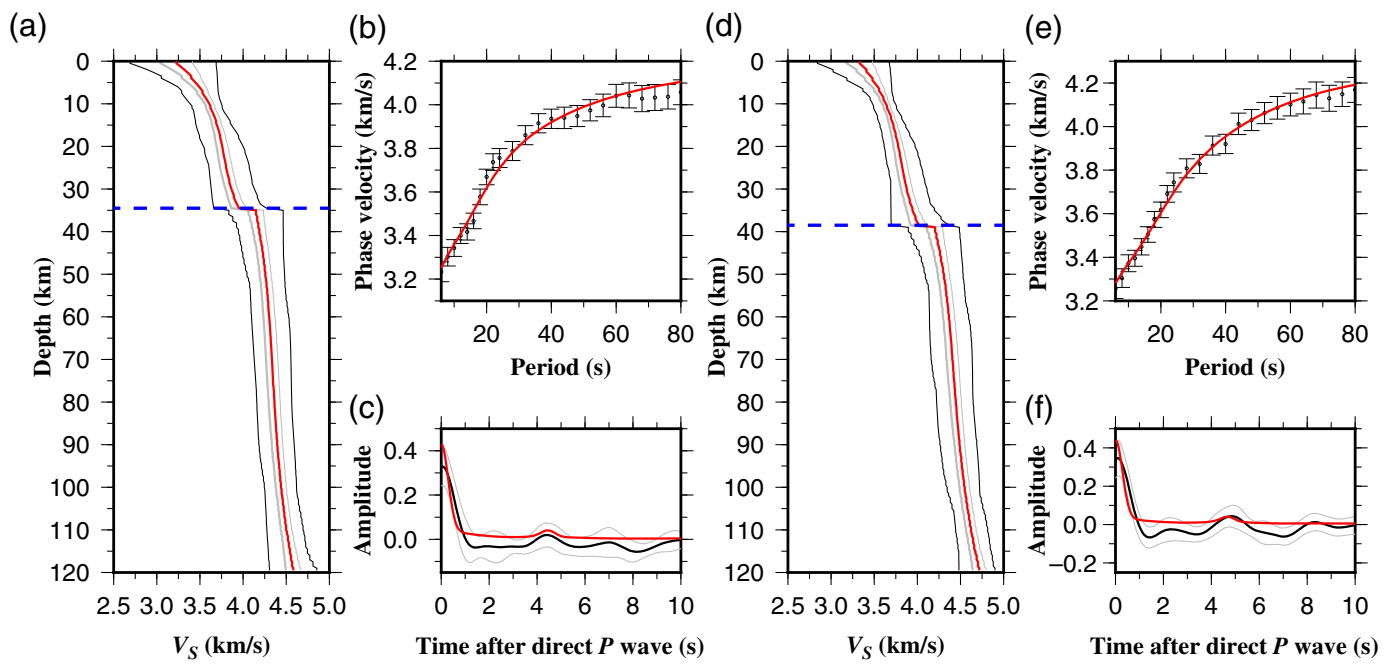
Crustal thickness measurements

Crustal thickness results were obtained separately from the H - V_p/V_s RF stacking (Fig. 7a) and joint inversion (Fig. 7b) approaches. For H measurements from the joint inversion, we searched for the largest velocity gradient in the 1D shear-wave velocity curve for the depth range of 20–60 km beneath each of the seismic stations. The resulting H distributions from the two

Figure 4. Distributions of Rayleigh-wave phase velocities at different periods. (a–c) 6, 12, and 24 s, from the EGF analysis, respectively. (d–f) 40, 60, and 80 s, from the TS analysis, respectively. V_{ph} , phase velocity. The color version of this figure is available only in the electronic edition.

methods are comparable with each other (Fig. 7c), with a mean difference of 1.2 ± 0.7 km and an absolute mean difference value of 1.3 ± 0.6 km.

The H measurements from the H - V_p/V_s RF stacking were used for generating initial models for the inversion, and the H values discussed subsequently were from the joint inversion. H measurements range from 26.0 km at station KGMA located within the western branch of the EARS to 46.0 km at station CRTR to the north of the MRS, with an average value of 36.2 ± 3.2 km (Fig. 7b). The TC has a mean H of 37.0 ± 2.2 km, which



is typical for cratons (e.g., Clitheroe *et al.*, 2000; Nair *et al.*, 2006). Small H measurements are mainly found along the two branches except for the southern TRS and northern MRS, whereas large H values are measured beneath the orogenic belts with a mean value of ~ 40 km.

Crustal V_p/V_s measurements

The mean crustal V_p/V_s measurement from the H - V_p/V_s RF stacking analysis is 1.81 ± 0.06 with the minimum value of 1.70 at station BOBN in the Kivu Volcanic Province and the maximum value of 1.97 at station NG56 in the southernmost tip of the KRS (Fig. 7d). With the exception of the Kivu Volcanic Province and a small portion of the rift shoulders of the KRS, the western and eastern branches are characterized by relatively high (>1.81) V_p/V_s measurements, especially for the central and southern TRS and the Rungwe Volcanic Province, where the mean crustal V_p/V_s value is greater than 1.85. The Kivu Volcanic Province and parts of the southern KRS rift shoulders possess the lowest (<1.73) V_p/V_s values in the entire study region. Spatially continuous images for the resulting velocities, H , and crustal V_p/V_s (Figs. 6–8) were produced by utilizing a continuous curvature surface gridding algorithm with a tension factor of 0.25 and an interval of 0.1° (Smith and Wessel, 1990). Areas with a distance $\geq 0.5^\circ$ from the nearest station are masked.

Discussion

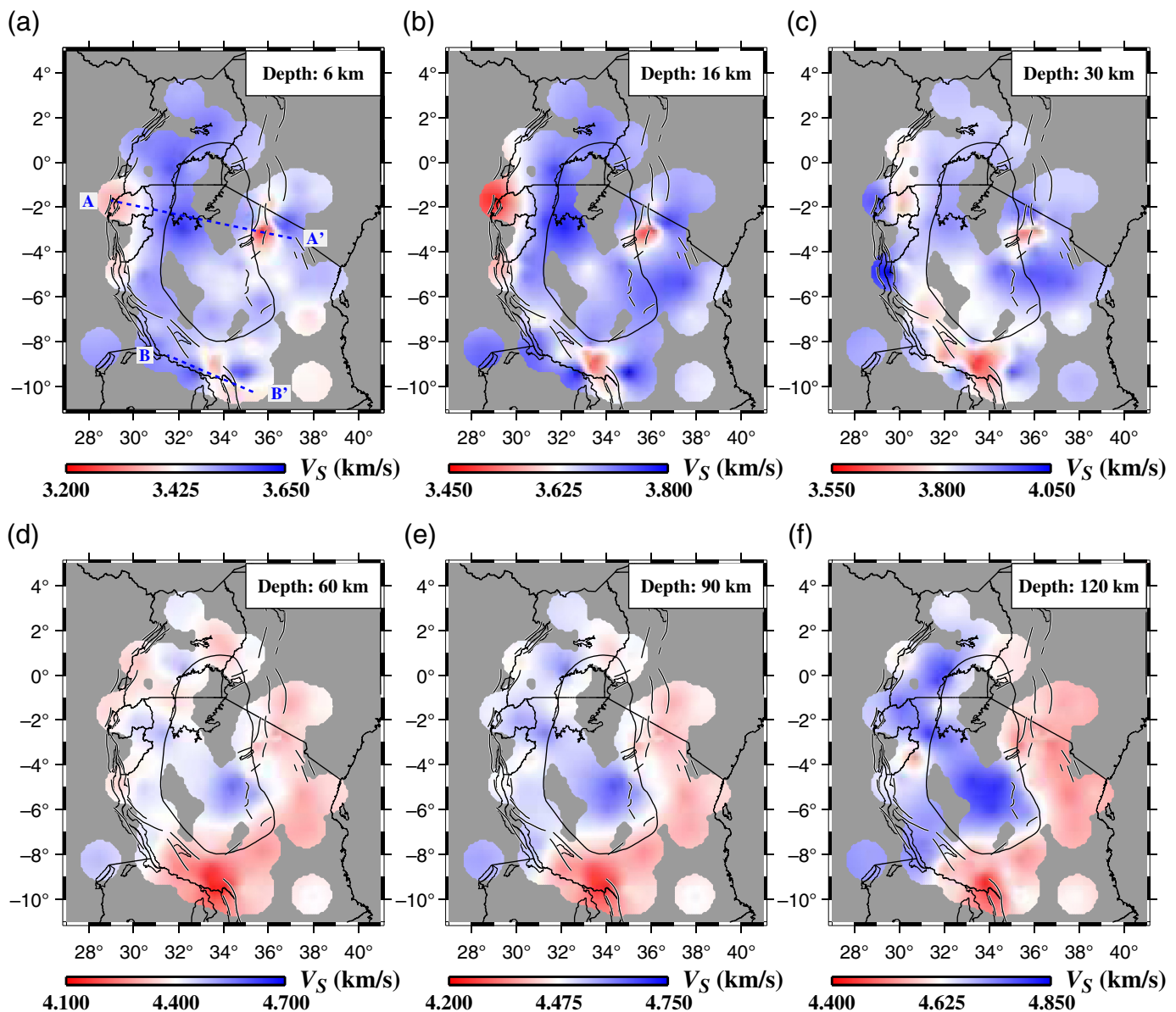
A mafic lower crustal layer beneath the TC

A high-velocity layer (~ 2 – 4 km thick) beneath the southern portion of the TC with V_s up to ~ 4.1 km/s was previously revealed by a tomography study (Julia *et al.*, 2005) and was suggested to be associated with a mafic lower crustal layer

Figure 5. Joint inversion results for (a–c) station AMBA and (d–f) station DODT. Locations for both stations are marked in Figure 2a. (a) Model ensemble for station AMBA using the Bayesian Monte Carlo joint inversion approach. The two black curves enclose the full width of the ensemble, and the two light gray curves enclose the 1σ width of the ensemble under the assumption of Gaussian distribution. The red curve in the model ensemble represents the average of all the accepted models. The Moho beneath the station is marked by the blue dashed line by searching the greatest velocity gradient. (b) Comparison between the observed Rayleigh-wave phase velocity measurements (black dots with 1σ error bars) and the prediction (red curve) from the best fitting in (a). (c) Comparison between the stacked RF trace (black curve with 1σ uncertainties) and the predicted RF trace (red curve) from the best fitting in (a). (d–f) Description of the same contents as those for (a–c) but for station DODT. The color version of this figure is available only in the electronic edition.

probably from emplacement of mantle-derived materials (e.g., Halls *et al.*, 1987; Kabete *et al.*, 2012; Thomas *et al.*, 2016). This interpretation is supported by our velocity model, which shows a mean shear-wave velocity of 3.86 ± 0.07 km/s in the lower crust (Fig. 8b) at the eight stations in the southern TC. The mean velocity is $\sim 2.9\%$ higher than that in the IASP91 model (Kennett and Engdahl, 1991) for the same depth range. Besides, our resulting mean crustal V_p/V_s value of 1.80 ± 0.04 calculated from all the eight stations within the southern TC (Fig. 7d) also suggests a more mafic crust comparing with the global averaged value of 1.78 (Christensen, 1996), providing additional evidence for the presence of a mafic lower crustal layer.

In addition to the southern TC, our results indicate that the mafic lower crustal layer may also exist beneath the northern



TC. The mean lower crustal shear velocity computed from the four stations in the northern TC is 3.91 ± 0.08 km/s, which is even higher than that of the southern TC and is $\sim 4.3\%$ higher than the IASP91 model, and the mean crustal V_P/V_S value of 1.80 ± 0.06 for the four stations is comparable to that in the southern TC (Fig. 7d). The observations of higher-than-normal lower crustal velocity and crustal V_P/V_S values of the TC suggest that a lower crustal mafic layer exists beneath the entire TC.

Crustal partial melting beneath the EARS

High crustal V_P/V_S measurements are obtained beneath the southern KRS (1.83 ± 0.08 from 11 stations within the region; open circles in Fig. 7d), the central and southern parts of the TRS (1.86 ± 0.04 from five stations; open diamonds in Fig. 7d), and the Rungwe Volcanic Province (1.87 ± 0.04 from 12 stations; open squares in Fig. 7d). Comparing with the mean value

Figure 6. Shear velocity slices at different depths. (a) 6, (b) 16, (c) 30, (d) 60, (e) 90, and (f) 120 km. The color version of this figure is available only in the electronic edition.

of 1.78 for continental crust (Christensen, 1996), our crustal V_P/V_S measurements for these three regions are elevated by $\sim 2.8\%$, $\sim 5.0\%$, and $\sim 4.5\%$, respectively. Several factors may contribute to the higher-than-normal crustal V_P/V_S values. First, the existence of basaltic sediments atop the crust might increase the crustal V_P/V_S values. The KRS, one of the most volcanically prolific Phanerozoic continental rifts on Earth, has a total volume of $\sim 230,000$ km³ volcanic rocks (King, 1978). Sitting between the TRS and MRS, the Rungwe Volcanic Province has erupted in the past 10 Ka and continuously accumulates basaltic sediments (Ebinger *et al.*, 1989). The contribution of the surface basaltic layer to the observed

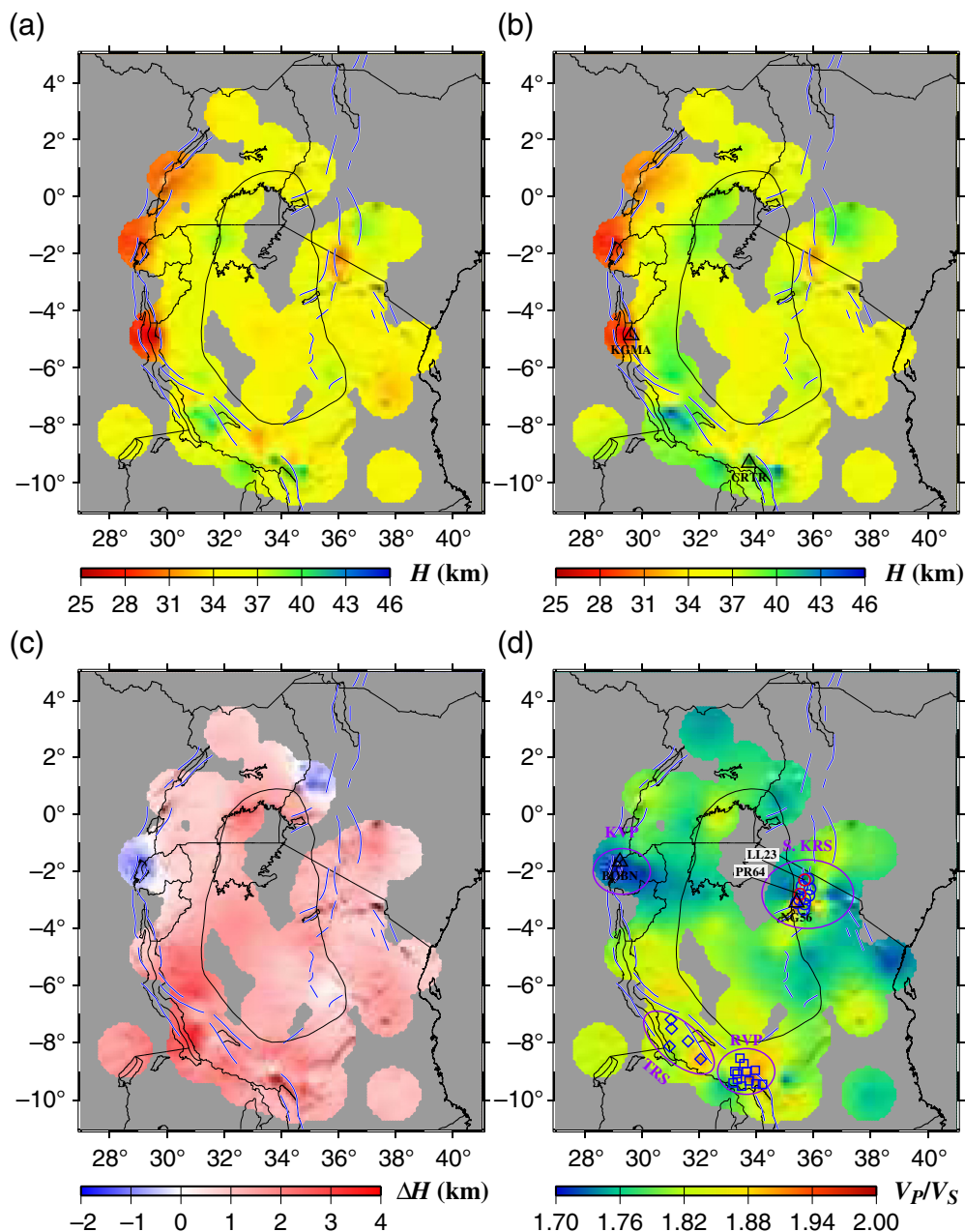


Figure 7. Crustal thickness (H) and V_p/V_s measurements. (a) H measurements from the H - V_p/V_s RF stacking approach. (b) H measurements from the joint Monte Carlo inversion approach. (c) Difference between results shown in (a) and (b). (d) Crustal V_p/V_s measurements from the H - V_p/V_s RF stacking. The small open circles represent stations used for calculating mean crustal V_p/V_s value within the rift valley of the southern Kenya rift segment, diamonds for the Tanganyika rift segment, and squares for the Rungwe Volcanic Province. The two red open circles represent stations with low crustal V_p/V_s values within the southern Kenya rift segment. KVP, Kivu Volcanic Province; RVP, Rungwe Volcanic Segment; S, KRS, southern Kenya rift segment; TRS, Tanganyika rift segment. The color version of this figure is available only in the electronic edition.

high crustal V_p/V_s values is limited, however. If we assume that the V_p/V_s value for solid basalts is 1.84 (Christensen, 1996), the crustal V_p/V_s would only be elevated to ~ 1.79 from 1.78 for a 35-km-thick crust (e.g., Kennett and Engdahl, 1991) with a 7-km-thick basalt layer (e.g., Morley, 1988).

The second possible factor that contributes to the elevated crustal V_p/V_s measurements observed in the two branches of the EARS is magmatic intrusion from the mantle. Besides the volcanically active KRS and Rungwe Volcanic Province, magmatic intrusion is also proposed beneath the nonvolcanic TRS (Hodgson *et al.*, 2017). The observed mean crustal V_p/V_s values for these segments are between 1.83 and 1.87, which are either comparable to or higher than the value of 1.84 for solid basalts (Christensen, 1996), suggesting that basaltic intrusion cannot fully account for the anomalously high crustal V_p/V_s measurements, even for the unlikely scenario when most or all of the original crustal material was replaced by basaltic intrusions. Other processes such as crustal partial melting are required to explain the high crustal V_p/V_s measurements. It has been proposed that crustal V_p/V_s is a continuous function of melt fraction (Watanabe, 1993). For silicates in the crust, V_p/V_s is 1.82 for 0% melt, and it increases to 1.90 for 5% melt and 2.05 for 10% melt (Watanabe, 1993). Therefore, a few percent of crustal melting is required to account for the observed high crustal V_p/V_s in various segments of the EARS.

CO₂-filled fractures beneath segments of the EARS

Lower-than-normal crustal V_p/V_s and shear velocity values are observed at many of the stations in the southern terminus area of the KRS (Figs. 7d and 8a,b). At approximately the same location, Roecker *et al.* (2017) report low V_p/V_s values in the upper crust based on seismic tomography inversions, and they attribute both the low V_p/V_s values and low

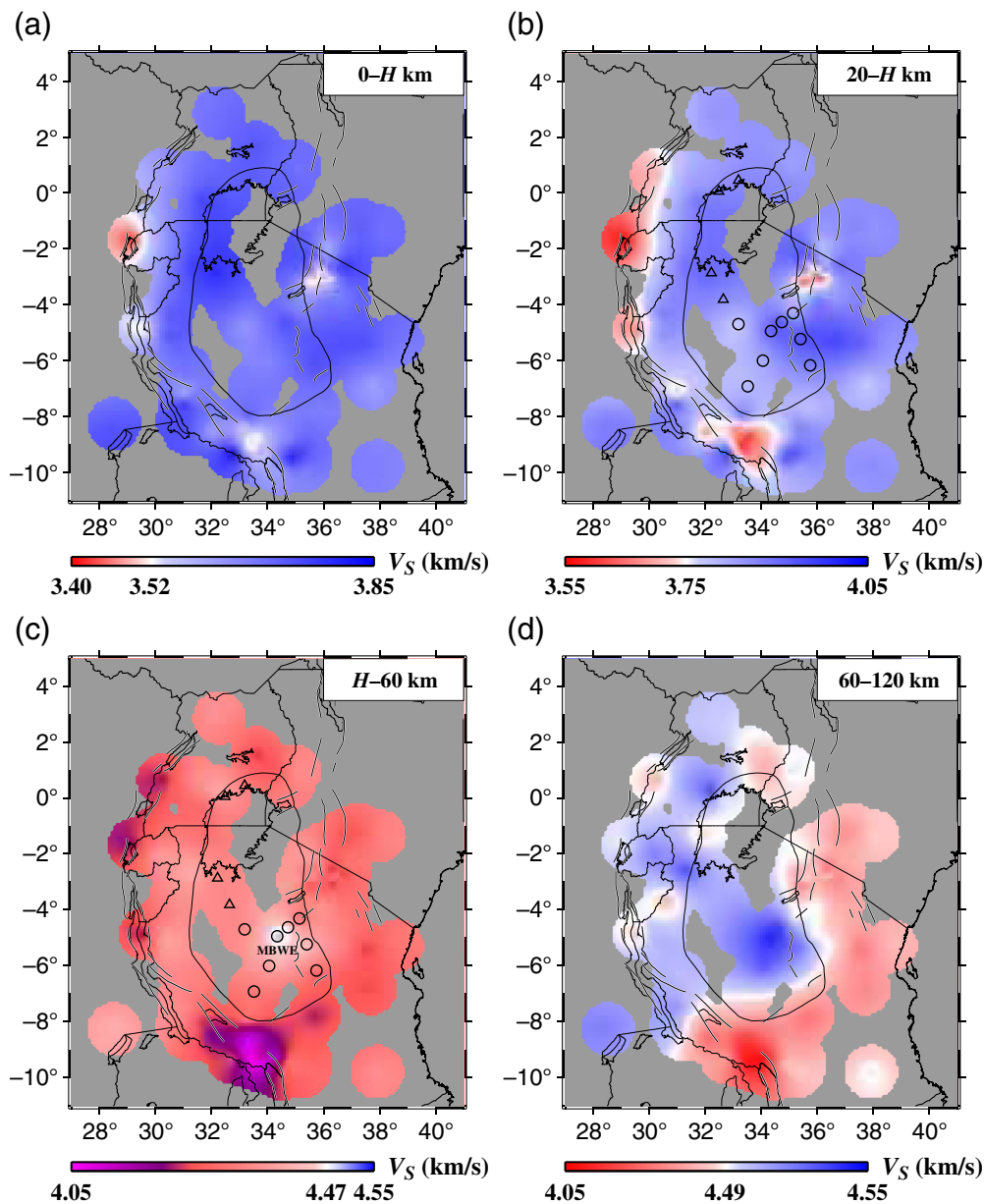


Figure 8. Mean shear-wave velocities for different depth ranges. White areas indicate mean shear-wave velocities calculated from the IASP91 model. (a) Between the surface and the Moho. (b) Between 20 km depth and the Moho. (c) Between the Moho and 60 km depth. (d) Between 60 and 120 km depth. In (b) and (c), open triangles represent the four stations located in the northern part of the craton, whereas the open circles represent the eight stations in the southern part. The color version of this figure is available only in the electronic edition.

velocities in the upper crust to volcanic plumbing suffused by CO_2 . Within the rift valley, we observed an extremely low crustal V_P/V_S value of 1.73 at station LL23 (Fig. 7d). The observation agrees with results of Roeker *et al.* (2017), which show low V_P/V_S values through the upper and mid crust at the station with the exception for the depth of 10 km. Roeker *et al.* (2017) indicate that the lowest V_P/V_S values are along both the western and eastern boundaries of the rift zone, whereas our lowest crustal V_P/V_S measurement of 1.72 is observed at

station PR64 near the western boundary of the rift zone (Fig. 7d). The RF study by Plasman *et al.* (2017) also shows relatively low crustal V_P/V_S values at stations LL23 (1.71) and PR64 (1.67), and their results are generally in agreement with our resulting crustal V_P/V_S distribution in this region (Fig. 7d).

The same mechanism may also be applicable to the Kivu Volcanic Province in the western branch, where an extremely low crustal V_P/V_S value of ~ 1.70 (the lowest value within the entire study area) is observed at station BOBN (Fig. 7d). We speculate that the low velocities in the lower crust and/or uppermost mantle (Fig. 8b,c) are caused by molten rock repository, which releases gaseous CO_2 leading to the low crustal V_P/V_S value in the region. Such a hypothesis is consistent with the large volume of CO_2 observed on the surface in the vicinity of that region (Balagizi *et al.*, 2015). CO_2 -related low velocities and V_P/V_S values are also suggested beneath other volcanic zones in the world (e.g., Lin *et al.*, 2014 for the Kilauea Volcano and Sun *et al.*, 2021 for the MRS south of the study area).

Low shear velocities in the uppermost mantle beneath the region

Our velocity model suggests the presence of low shear velocities beneath the Moho of the study region, with the lowest velocities of ~ 4.10 km/s found beneath the Kivu, Rungwe, and Virunga volcanic provinces in the western branch (Fig. 8c). These low velocities are in general agreement with results from other surface-wave tomography studies (O'Donnell *et al.*, 2013; Accardo *et al.*, 2017; Adams *et al.*, 2018). We similarly interpret the low velocities in the uppermost mantle beneath the three volcanic provinces as reflecting magmatic upwelling associated with the volcanisms. The

effective elastic thickness (T_e) of the African lithosphere measured by Perez-Gussinye *et al.* (2009) shows that the volcanic provinces possess low- T_e values, indicating the possible presence of conduits in the lithosphere that provide hot materials from the asthenosphere (Perez-Gussinye *et al.*, 2009).

The low velocities beneath the other parts of the region can be explained by the pervasive existence of underplating, a process that produces a layer of mantle-derived magma trapped and spread horizontally below the Moho (e.g., Cox, 1993). The average elevation of the East African plateau is ~1000 m (Nyblade and Robinson, 1994; Mulibo and Nyblade, 2013a), and that of the TC, which is located in the central part of the plateau, is 1260 m (Weeraratne *et al.*, 2003). A previous RF and surface-wave tomography study speculates that low densities in the mantle, if present, are responsible for the isostatic uplift of the East African plateau (Last *et al.*, 1997). The hypothesis is supported by a gravity modeling study of the eastern TC and parts of the eastern branch (Fletcher *et al.*, 2018) and by tomography studies imaging a low velocity zone in the upper mantle beneath the TC (Weeraratne *et al.*, 2003; Sebai *et al.*, 2006). Dynamic topography associated with a mantle plume beneath the East African plateau has also been invoked to explain the uplift and rifting in the region (e.g., Simiyu and Keller, 1997; Ebinger and Sleep, 1998). Weeraratne *et al.* (2003) image a relatively reduced seismic velocity zone in the uppermost mantle beneath the East African plateau, although the actual velocities are still higher than global average values and our inverted results. The TX2019slab velocity model (Lu *et al.*, 2019) suggests that the northern portion of the Archean craton is characterized by lower-than-normal shear velocities in the uppermost mantle, whereas the velocities in the southern portion are mostly higher than normal. Although controversies among the studies might be the results of the different techniques and the initial models used by the studies, the low velocity and presumably low-density layer in the uppermost mantle revealed from this study may contribute to the uplift of the TC.

Conclusions

A 3D shear-wave velocity model for the upper 120 km beneath the TC and adjacent orogenic belts and the eastern and western branches of the EARS is constructed using a nonlinear Bayesian Monte Carlo joint inversion of RFs and Rayleigh-wave phase velocity dispersion. The observations provide constraints to a number of significant geological problems regarding continental lithospheric structure and evolution. The previously proposed lower crustal mafic layer in the southern portion of the TC is confirmed by our results, and our new results suggest that this mafic layer also exists beneath the northern portion of the craton. Beneath the western and eastern branches of the EARS, the observed high crustal V_p/V_s can be interpreted as a combination of a basaltic layer atop the crust, magmatic intrusion from the mantle, and the

existence of crustal partial melting. Low seismic velocities and crustal V_p/V_s measurements observed beneath the Kivu Volcanic Province and the southern KRS can be attributed to CO₂-filled magma conduits or fractures. Low velocities are imaged in the uppermost mantle beneath almost the entire study region, which can be interpreted by the existence of magmatic underplating beneath the region and may contribute to the uplift of the TC.

Data and Resources

All the broadband seismic data used in the present study were obtained from the Incorporated Research Institutions for Seismology Data Management Center (IRIS-DMC) and are publicly accessible (<https://ds.iris.edu/ds/nodes/dmc>, last accessed May 2019). The stations that recorded the data are part of the following seismic networks: (1) AF (2004–present; Penn State University, 2004); (2) IU (1988–present; Albuquerque Seismological Laboratory (ASL)/USGS, 1988); (3) XD (1994–1995; Owens and Nyblade, 1994); (4) XI (2000–2002; Nyblade, 2000); (5) XJ (2013–2015; Ebinger, 2013); (6) XW (2017–2018; Nyblade, 2017); (7) YH (2010–2011; Nyblade, 2010); (8) YQ (2013–2016; Gaherty *et al.*, 2013); (9) ZP (2007–2009; Nyblade, 2007); and (10) ZV (2014–2015; Ebinger, 2014). Figures were generated with the Generic Mapping Tools (GMT; Wessel and Smith, 1998).

Declaration of Competing Interests

The authors acknowledge that there are no conflicts of interest recorded.

Acknowledgments

The facilities of Incorporated Research Institutions for Seismology (IRIS) Data Services, and specifically the IRIS Data Management Center (DMC), were used for access to waveforms and related metadata used in this study. IRIS Data Services are funded through the Seismological Facilities for the Advancement of Geoscience (SAGE) Award of the National Science Foundation (NSF) under Cooperative Support Agreement EAR-1851048. The authors thank Brandon Schmandt and an anonymous reviewer for constructive reviews that significantly improved the article. The study was partially supported by the U.S. NSF under Grants 1009946 to K. L. and S. G., 1919789 to S. G., and the American Chemical Society under Grant PRF-60281-ND8 to S. G.

References

- Accardo, N. J., J. B. Gaherty, D. J. Shillington, C. J. Ebinger, A. A. Nyblade, G. J. Mbogoni, P. R. N. Chindandali, R. W. Ferdinand, G. D. Mulibo, G. Kamihanda, *et al.* (2017). Surface wave imaging of the weakly extended Malawi Rift from ambient-noise and teleseismic Rayleigh waves from onshore and lake-bottom seismometers, *Geophys. J. Int.* **209**, no. 3, 1892–1905, doi: [10.1093/gji/ggx133](https://doi.org/10.1093/gji/ggx133).
- Accardo, N. J., J. B. Gaherty, D. J. Shillington, E. Hopper, A. A. Nyblade, C. J. Ebinger, C. A. Scholz, P. R. N. Chindandali, R. Wambura-Ferdinand, G. Mbogoni, *et al.* (2020). Thermochemical modification of the upper mantle beneath the northern Malawi rift constrained from shear velocity imaging, *Geochem. Geophys. Geosys.* **21**, no. 6, e2019GC008843, doi: [10.1029/2019GC008843](https://doi.org/10.1029/2019GC008843).

- Achauer, U., and The KRISP Teleseismic Working Group (1994). New ideas on the Kenya rift based on the inversion of the combined dataset of the 1985 and 1989/90 seismic tomography experiments, *Tectonophysics* **236**, nos. 1/4, 305–329, doi: [10.1016/0040-1951\(94\)90182-1](https://doi.org/10.1016/0040-1951(94)90182-1).
- Adams, A., J. Miller, and N. Accardo (2018). Relationships between lithospheric structures and rifting in the East African Rift System: A Rayleigh wave tomography study, *Geochem. Geophys. Geosys.* **19**, no. 10, 3793–3810, doi: [10.1029/2018GC007750](https://doi.org/10.1029/2018GC007750).
- Albuquerque Seismological Laboratory (ASL)/USGS (1988). Global seismograph network—IRIS/USGS, *International Federation of Digital Seismograph Networks, Dataset/Seismic Network*, doi: [10.7914/SN/IU](https://doi.org/10.7914/SN/IU).
- Bagley, B., and A. A. Nyblade (2013). Seismic anisotropy in eastern Africa, mantle flow, and the African superplume, *Geophys. Res. Lett.* **40**, no. 8, 1500–1505, doi: [10.1002/grl.50315](https://doi.org/10.1002/grl.50315).
- Balagizi, C. M., F. Darchambeau, S. Bouillon, M. M. Yalire, T. Lambert, and A. V. Borges (2015). River geochemistry, chemical weathering, and atmospheric CO₂ consumption rates in the Virunga Volcanic Province (East Africa), *Geochem. Geophys. Geosys.* **16**, no. 8, 2637–2660, doi: [10.1002/2015GC005999](https://doi.org/10.1002/2015GC005999).
- Bensen, G. D., M. H. Ritzwoller, M. P. Barmin, A. L. Levshin, F. Lin, M. P. Moschetti, N. M. Shapiro, and Y. Yang (2007). Processing seismic ambient noise data to obtain reliable broad-band surface wave dispersion measurements, *Geophys. J. Int.* **169**, 1239–1260, doi: [10.1111/j.1365-246X.2007.03374.x](https://doi.org/10.1111/j.1365-246X.2007.03374.x).
- Cahen, L., N. Snelling, J. Delhal, and J. Vail (1984). *The Geochronology and Evolution of Africa*, Oxford University Press, New York, New York.
- Christensen, N. I. (1996). Poisson's ratio and crustal seismology, *J. Geophys. Res.* **101**, no. B2, 3139–3156, doi: [10.1029/95JB03446](https://doi.org/10.1029/95JB03446).
- Clayton, R. W., and R. A. Wiggins (1976). Source shape estimation and deconvolution of teleseismic bodywaves, *Geophys. J. Int.* **47**, no. 1, 151–177, doi: [10.1111/j.1365-246X.1976.tb01267.x](https://doi.org/10.1111/j.1365-246X.1976.tb01267.x).
- Clitheroe, G., O. Gudmundsson, and B. L. N. Kennett (2000). The crustal thickness of Australia, *J. Geophys. Res.* **105**, no. B6, 13,697–13,713, doi: [10.1029/1999JB900317](https://doi.org/10.1029/1999JB900317).
- Cox, K. G. (1993). Continental magmatic underplating, *Phil. Trans. Roy. Soc. Lond. A* **342**, no. 1663, 155–166, doi: [10.1098/rsta.1993.0011](https://doi.org/10.1098/rsta.1993.0011).
- Dugda, M. T., A. A. Nyblade, J. Julia, C. A. Langston, C. J. Ammon, and S. Simiyu (2005). Crustal structure in the Ethiopia and Kenya from receiver function analysis: Implications for rift development in eastern Africa, *J. Geophys. Res.* **110**, no. B1, 1–15, doi: [10.1029/2004JB003065](https://doi.org/10.1029/2004JB003065).
- Ebinger, C. (2013). Magadi-Natron magmatic rifting studies, *International Federation of Digital Seismograph Networks, Dataset/Seismic Network*, doi: [10.7914/SN/XJ_2013](https://doi.org/10.7914/SN/XJ_2013).
- Ebinger, C. (2014). Southern lake Tanganyika experiment, *International Federation of Digital Seismograph Networks, Dataset/Seismic Network*, doi: [10.7914/SN/ZV_2014](https://doi.org/10.7914/SN/ZV_2014).
- Ebinger, C. J., and N. H. Sleep (1998). Cenozoic magmatism throughout east Africa resulting from impact of a single plume, *Nature* **395**, no. 6704, 788–791, doi: [10.1038/27417](https://doi.org/10.1038/27417).
- Ebinger, C. J., A. L. Deino, R. E. Drake, and A. L. Tesha (1989). Chronology of volcanism and rift basin propagation: Rungwe Volcanic Province, East Africa, *J. Geophys. Res.* **94**, no. B11, 15,785–15,803, doi: [10.1029/JB094iB11p15785](https://doi.org/10.1029/JB094iB11p15785).
- Efron, B., and R. Tibshirani (1986). Bootstrap methods for standard errors, confidence intervals, and other measures of statistical accuracy, *Stat. Sci.* **1**, no. 1, 54–75, doi: [10.1214/ss/1177013815](https://doi.org/10.1214/ss/1177013815).
- Fishwick, S. (2010). Surface wave tomography: Imaging of the lithosphere-asthenosphere boundary beneath central and southern Africa? *Lithos* **120**, no. 1/2, 63–73, doi: [10.1016/j.lithos.2010.05.011](https://doi.org/10.1016/j.lithos.2010.05.011).
- Fletcher, A. W., M. G. Abdelsalam, L. Emishaw, E. A. Atekwana, D. A. Lao-Davila, and A. Ismail (2018). Lithospheric controls on the rifting of the Tanzanian Craton at the Eyasi Basin, Eastern Branch of the East African Rift System, *Tectonics* **37**, no. 9, 2818–2832, doi: [10.1029/2018TC005065](https://doi.org/10.1029/2018TC005065).
- Gaherty, J., C. Ebinger, A. Nyblade, and D. Shillington (2013). Study of extension and magmatism in Malawi and Tanzania, *International Federation of Digital Seismograph Networks, Dataset/Seismic Network*, doi: [10.7914/SN/YQ_2013](https://doi.org/10.7914/SN/YQ_2013).
- George, R., N. Rogers, and S. Kelley (1998). Earliest magmatism in Ethiopia: Evidence for two mantle plumes in one flood basalt province, *Geology* **26**, no. 10, 923–926, doi: [10.1130/0091-7613\(1998\)026<0923:EMIEEF>2.3.CO;2](https://doi.org/10.1130/0091-7613(1998)026<0923:EMIEEF>2.3.CO;2).
- Green, W. V., U. Achauer, and R. P. Meyer (1991). A three-dimensional seismic image of the crust and upper mantle beneath the Kenya rift, *Nature* **354**, no. 6350, 119–203, doi: [10.1038/354199a0](https://doi.org/10.1038/354199a0).
- Halls, H. C., K. G. Burns, S. J. Bullock, and P. M. Batterham (1987). Mafic dyke swarms of Tanzania interpreted from aeromagnetic data, in *Mafic Dyke Swarms*, H. C. Halls and W. F. Fahrig (Editors), Geological Association of Canada, St John's, Newfoundland, Special Paper 34, 173–186.
- Hansen, S. E., A. A. Nyblade, and M. H. Benoit (2012). Mantle structure beneath Africa and Arabia from adaptively parameterized P-wave tomography: Implications for the origin of Cenozoic Afro-Arabian tectonism, *Earth Planet. Sci. Lett.* **319/320**, 23–34, doi: [10.1016/j.epsl.2011.12.023](https://doi.org/10.1016/j.epsl.2011.12.023).
- Hodgson, I., F. Illsley-Kemp, R. J. Gallacher, D. Keir, C. J. Ebinger, and K. Mtelega (2017). Crustal structure at a young continental rift: A receiver function study from the Tanganyika Rift, *Tectonics* **36**, no. 12, 2806–2822, doi: [10.1002/2017TC004477](https://doi.org/10.1002/2017TC004477).
- Julia, J., C. J. Ammon, and A. A. Nyblade (2005). Evidence for mafic lower crust in Tanzania, East Africa, from joint inversion of receiver functions and Rayleigh wave dispersion velocities, *Geophys. J. Int.* **162**, no. 2, 555–569, doi: [10.1111/j.1365-246X.2005.02685.x](https://doi.org/10.1111/j.1365-246X.2005.02685.x).
- Kabete, J. M., D. I. Groves, N. J. McNaughton, and A. H. Mruma (2012). A new tectonic and framework for the Tanzania Shield: Implications for gold metallogeny and undiscovered endowment, *Ore Geol. Rev.* **48**, 88–124, doi: [10.1016/j.oregeorev.2012.02.009](https://doi.org/10.1016/j.oregeorev.2012.02.009).
- Kampunzu, A., M. Bonhmmme, and M. Kanika (1998). Geochronology of volcanic rocks and evolution of the Cenozoic western branch of the East Africa Rift System, *J. Afr. Erath Sci.* **26**, no. 3, 441–461, doi: [10.1016/S0899-5362\(98\)00025-6](https://doi.org/10.1016/S0899-5362(98)00025-6).
- Kennett, B. L. N., and E. R. Engdahl (1991). Traveltimes for global earthquake location and phase identification, *Geophys. J. Int.* **105**, no. 2, 429–465, doi: [10.1111/j.1365-246X.1991.tb06724.x](https://doi.org/10.1111/j.1365-246X.1991.tb06724.x).
- King, B. C. (1978). Structural and volcanic evolution of the Gregory Rift Valley, *Geol. Soc. Lond. Spec. Publ.* **6**, no. 1, 29–54, doi: [10.1144/GSL.SP.1978.006.01.05](https://doi.org/10.1144/GSL.SP.1978.006.01.05).
- Kong, F., S. S. Gao, K. H. Liu, W. Ding, and J. Li (2020). Slab dehydration and mantle upwelling in the vicinity of the Sumatra

- subduction zone: Evidence from receiver function imaging of mantle transition zone discontinuities, *J. Geophys. Res.* **125**, e2020JB019381, doi: [10.1029/2020JB019381](https://doi.org/10.1029/2020JB019381).
- Last, R. J., A. A. Nyblade, C. A. Langston, and T. J. Owens (1997). Crustal structure of the East African Plateau from receiver functions and Rayleigh wave phase velocities, *J. Geophys. Res.* **102**, no. B11, 24,469–24,483, doi: [10.1029/97JB02156](https://doi.org/10.1029/97JB02156).
- Lee, H., J. D. Muirhead, T. P. Fischer, C. J. Ebinger, S. A. Kattenhorn, Z. D. Sharp, and G. Kianji (2016). Massive and prolonged deep carbon emissions associated with continental rifting, *Nat. Geosci.* **9**, 145–149, doi: [10.1038/NNGEO2622](https://doi.org/10.1038/NNGEO2622).
- Lin, G., P. M. Shearer, R. S. Matoza, P. G. Okubo, and F. Amelung (2014). Three-dimensional seismic velocity structure of Mauna Loa and Kilauea volcanoes in Hawaii from local seismic tomography, *J. Geophys. Res.* **119**, no. 5, 4377–4392, doi: [10.1002/2013JB010820](https://doi.org/10.1002/2013JB010820).
- Liu, K. H., and S. S. Gao (2010). Spatial variations of crustal characteristics beneath the Hoggar swell, Algeria, revealed by systematic analyses of receiver functions from a single seismic station, *Geochem. Geophys. Geosys.* **11**, no. 8, Q08011, doi: [10.1029/2010GC003091](https://doi.org/10.1029/2010GC003091).
- Lu, C., S. P. Grand, H. Lai, and E. J. Garnero (2019). TX2019slab: A new P and S tomography model incorporating subducting slabs, *J. Geophys. Res.* **124**, no. 11, 11,549–11,567, doi: [10.1029/2019JB017448](https://doi.org/10.1029/2019JB017448).
- Montagner, J.-P. (1986). Regional three-dimensional structures using long period surface waves, *Ann. Geophys.* **4**, no. 3, 283–294.
- Morley, C. K. (1988). Variable extension in Lake Tanganyika, *Tectonics* **7**, no. 4, 785–801, doi: [10.1029/TC007i004p00785](https://doi.org/10.1029/TC007i004p00785).
- Mulibo, G. D., and A. A. Nyblade (2013a). The P and S wave velocity structure of the mantle beneath eastern Africa and the African superplume anomaly, *Geochem. Geophys. Geosys.* **14**, no. 8, 2696–2715, doi: [10.1002/ggge.20150](https://doi.org/10.1002/ggge.20150).
- Mulibo, G. D., and A. A. Nyblade (2013b). Mantle transition zone thinning beneath eastern Africa: Evidence for a whole-mantle superplume structure, *Geophys. Res. Lett.* **40**, no. 14, 3562–3566, doi: [10.1002/grl.50694](https://doi.org/10.1002/grl.50694).
- Nair, S. K., S. S. Gao, K. H. Liu, and P. G. Silver (2006). Southern African crustal evolution and composition: Constraints from receiver function studies, *J. Geophys. Res.* **111**, no. 2, doi: [10.1029/2005JB003802](https://doi.org/10.1029/2005JB003802).
- Nyblade, A. (2000). Seismic investigation of deep structure beneath the Ethiopian Plateau and Afar Depression, *International Federation of Digital Seismograph Networks, Dataset/Seismic Network*, doi: [10.7914/SN/XI_2000](https://doi.org/10.7914/SN/XI_2000).
- Nyblade, A. (2007). AfricaArray-Uganda/Tanzania, *International Federation of Digital Seismograph Networks, Dataset/Seismic Network*, doi: [10.7914/SN/ZP_2007](https://doi.org/10.7914/SN/ZP_2007).
- Nyblade, A. (2010). AfricaArray SE Tanzania basin experiment, *International Federation of Digital Seismograph Networks, Dataset/Seismic Network*, doi: [10.7914/SN/YH_2010](https://doi.org/10.7914/SN/YH_2010).
- Nyblade, A. (2017). Broadband Seismic experiment in NE Uganda to investigate plume-lithosphere interactions, *International Federation of Digital Seismograph Networks, Dataset/Seismic Network*, doi: [10.7914/SN/XW_2017](https://doi.org/10.7914/SN/XW_2017).
- Nyblade, A. A., and S. W. Robinson (1994). The African superswell, *Geophys. Res. Lett.* **21**, no. 9, 765–768, doi: [10.1029/94GL00631](https://doi.org/10.1029/94GL00631).
- O'Donnell, J. P., A. Adams, A. A. Nyblade, G. D. Mulibo, and F. Tugume (2013). The uppermost mantle shear wave velocity structure of eastern Africa from Rayleigh wave tomography: constraints on rift evolution, *Geophys. J. Int.* **194**, no. 2, 961–978, doi: [10.1093/gji/ggt135](https://doi.org/10.1093/gji/ggt135).
- O'Donnell, J. P., K. Selway, A. A. Nyblade, R. A. Brazier, and N. El Tahir (2016). Thick lithosphere, deep crustal earthquakes and no melt: a triple challenge to understanding extension in the western branch of the East African Rift, *Geophys. J. Int.* **204**, no. 2, 985–998, doi: [10.1093/gji/ggv492](https://doi.org/10.1093/gji/ggv492).
- Owens, T., and A. Nyblade (1994). Seismic investigations of the lithospheric structure of the Tanzanian Craton, *International Federation of Digital Seismograph Networks, Dataset/Seismic Network*, doi: [10.7914/SN/XD_1994](https://doi.org/10.7914/SN/XD_1994).
- Pasyanos, M. E., T. G. Masters, G. Laske, and Z. Ma (2014). LITHO1.0: An updated crust and lithospheric model of the Earth, *J. Geophys. Res.* **119**, no. 3, 2153–2173, doi: [10.1002/2013JB010626](https://doi.org/10.1002/2013JB010626).
- Penn State University (2004). AfricaArray, *International Federation of Digital Seismograph Networks, Dataset/Seismic Network*, doi: [10.7914/SN/AF](https://doi.org/10.7914/SN/AF).
- Perez-Gussinye, M., M. Metois, M. Fernandez, J. Verges, J. Fulla, and A. R. Lowry (2009). Effective elastic thickness of Africa and its relationship to other proxies for lithospheric structure and surface tectonics, *Earth Planet. Sci. Lett.* **287**, nos. 1/2, 152–167, doi: [10.1016/j.epsl.2009.08.004](https://doi.org/10.1016/j.epsl.2009.08.004).
- Plasman, M., C. Tiberi, C. Ebinger, S. Gautier, J. Albaric, S. Peyrat, J. Deverchere, B. Le Gall, P. Tarits, S. Roecker, *et al.* (2017). Lithospheric low-velocity zones associated with a magmatic segment of the Tanzania Rift, East Africa, *Geophys. J. Int.* **210**, no. 1, 465–481, doi: [10.1093/gji/ggx177](https://doi.org/10.1093/gji/ggx177).
- Ritzwoller, M. H., N. M. Shapiro, M. P. Barmin, and A. L. Levshin (2002). Global surface wave diffraction tomography, *J. Geophys. Res.* **107**, no. B12, ESE 4-1–ESE 4-13, doi: [10.1029/2002JB001777](https://doi.org/10.1029/2002JB001777).
- Roberts, E. M., N. J. Stevens, P. M. O'Connor, P. H. G. M. Dirks, M. D. Gottfried, W. C. Clyde, R. A. Armstrong, A. I. S. Kemp, and S. Hemming (2012). Initiation of the western branch of the East African Rift coeval with the eastern branch, *Nat. Geosci.* **5**, no. 4, 289–294, doi: [10.1038/ngeo1432](https://doi.org/10.1038/ngeo1432).
- Roecker, S., C. Ebinger, C. Tiberi, G. Mulibo, R. Ferdinand-Wambura, K. Mtelega, G. Kianji, A. Muzuka, S. Gautier, J. Albaric, *et al.* (2017). Subsurface images of the Eastern Rift, Africa, from the joint inversion of body waves, surface waves and gravity: Investigating the role of fluids in early-stage continental rifting, *Geophys. J. Int.* **210**, no. 2, 931–950, doi: [10.1093/gji/ggx220](https://doi.org/10.1093/gji/ggx220).
- Sebai, A., E. Stutzmann, J. -P. Montagner, D. Sicilia, and E. Beucler (2006). Anisotropic structure of the African upper mantle from Rayleigh and Love wave tomography, *Phys. Earth Planet. In.* **155**, nos. 1/2, 48–62, doi: [10.1016/j.pepi.2005.09.009](https://doi.org/10.1016/j.pepi.2005.09.009).
- Shapiro, N. M., and M. Campillo (2004). Emergence of broadband Rayleigh waves from correlations of the ambient seismic noise, *Geophys. Res. Lett.* **31**, no. 7, 1–4, doi: [10.1029/2004GL019491](https://doi.org/10.1029/2004GL019491).
- Shapiro, N. M., and M. H. Ritzwoller (2002). Monte-Carlo inversion for a global shear-velocity model of the crust and upper mantle, *Geophys. J. Int.* **151**, no. 1, 88–105, doi: [10.1046/j.1365-246X.2002.01742.x](https://doi.org/10.1046/j.1365-246X.2002.01742.x).
- Shen, W., M. H. Ritzwoller, V. Schulte-Pelkum, and F.-C. Lin (2013). Joint inversion of surface wave dispersion and receiver functions:

- A Bayesian Monte-Carlo approach, *Geophys. J. Int.* **192**, no. 2, 807–836, doi: [10.1093/gji/ggs050](https://doi.org/10.1093/gji/ggs050).
- Simiyu, S. M., and G. R. Keller (1997). An integrated analysis of lithospheric structure across the East African plateau based on gravity anomalies and recent seismic studies, *Tectonophysics* **278**, nos. 1/4, 291–313, doi: [10.1016/S0040-1951\(97\)00109-1](https://doi.org/10.1016/S0040-1951(97)00109-1).
- Smith, M. (1994). Stratigraphic and structural constraints on mechanisms of active rifting in the Gregory Rift, Kenya, *Tectonophysics* **236**, nos. 1/4, 3–22, doi: [10.1016/0040-1951\(94\)90166-X](https://doi.org/10.1016/0040-1951(94)90166-X).
- Smith, W. H. F., and P. Wessel (1990). Gridding with continuous curvature splines in tension, *Geophysics* **55**, no. 3, 293–305, doi: [10.1190/1.1442837](https://doi.org/10.1190/1.1442837).
- Spiegel, C., B. Kohn, D. Belton, and A. Gleadow (2007). Morphotectonic evolution of the central Kenya rift flanks: Implications for late Cenozoic environmental change in East Africa, *Geology* **35**, no. 5, 427–430, doi: [10.1130/g23108a.1](https://doi.org/10.1130/g23108a.1).
- Sun, M., K. H. Liu, X. Fu, and S. S. Gao (2017). Receiver function imaging of mantle transition zone discontinuities beneath the Tanzania Craton and adjacent segments of the East African Rift System, *Geophys. Res. Lett.* **44**, no. 24, 12,116–12,124, doi: [10.1002/2017GL075485](https://doi.org/10.1002/2017GL075485).
- Sun, M., S. S. Gao, K. H. Liu, K. Mickus, X. Fu, and Y. Yu (2021). Receiver function investigation of crustal structure in the Malawi and Luangwa Rift Zones and adjacent areas, *Gondwana Res.* **89**, 168–176, doi: [10.1016/j.gr.2020.08.015](https://doi.org/10.1016/j.gr.2020.08.015).
- Thomas, R. J., C. Spencer, A. M. Bushi, N. Baglow, N. Boniface, G. de Kock, M. S. A. Horstwood, L. Hollick, J. Jacobs, S. Kajara, *et al.* (2016). Geochronology of the central Tanzania Craton and its southern and eastern orogenic margins, *Precambrian Res.* **277**, 47–67, doi: [10.1016/j.precamres.2016.02.008](https://doi.org/10.1016/j.precamres.2016.02.008).
- Tsekhmistrenko, M., K. Sigloch, K. Hosseini, and G. Barruol (2021). A tree of Indo-African mantle plumes imaged seismic tomography, *Nat. Geosci.* **14**, no. 8, 612–619, doi: [10.1038/s41561-021-00762-9](https://doi.org/10.1038/s41561-021-00762-9).
- Tugume, F., A. Nyblade, and J. Julia (2012). Moho depths and Poisson's ratios of Precambrian crust in East Africa: Evidence for similarities in Archean and Proterozoic crustal structure, *Earth Planet. Sci. Lett.* **355/356**, 73–81, doi: [10.1016/j.epsl.2012.08.041](https://doi.org/10.1016/j.epsl.2012.08.041).
- Wang, T., J. Feng, K. H. Liu, and S. S. Gao (2019). Crustal structure beneath the Malawi and Luangwa rift zones and adjacent areas from ambient noise tomography, *Gondwana Res.* **67**, 187–198, doi: [10.1016/j.gr.2018.10.018](https://doi.org/10.1016/j.gr.2018.10.018).
- Watanabe, T. (1993). Effects of water and melt on seismic velocities and their application to characterization of seismic reflectors, *Geophys. Res. Lett.* **20**, no. 24, 2933–2936, doi: [10.1029/93GL03170](https://doi.org/10.1029/93GL03170).
- Weeraratne, D. S., D. W. Forsyth, K. M. Fischer, and A. A. Nyblade (2003). Evidence for an upper mantle plume beneath the Tanzanian craton from Rayleigh wave tomography, *J. Geophys. Res.* **108**, no. B9, doi: [10.1029/2002JB002273](https://doi.org/10.1029/2002JB002273).
- Wessel, P., and W. H. F. Smith (1998). New, improved version of generic mapping tools released, *Eos Trans. AGU* **79**, no. 47, 579–579, doi: [10.1029/98EO00426](https://doi.org/10.1029/98EO00426).
- Yao, H., R. D. van Der Hilst, and M. V. de Hoop (2006). Surface-wave array tomography in SE Tibet from ambient seismic noise and two-station analysis—I. Phase velocity maps, *Geophys. J. Int.* **166**, no. 2, 732–744, doi: [10.1111/j.1365-246X.2006.03028.x](https://doi.org/10.1111/j.1365-246X.2006.03028.x).
- Yao, H., R. D. van Der Hilst, and J.-P. Montagner (2010). Heterogeneity and anisotropy of the lithosphere of SE Tibet from surface wave array tomography, *J. Geophys. Res.* **115**, no. B12, doi: [10.1029/2009JB007142](https://doi.org/10.1029/2009JB007142).
- Yao, H., G. Xu, L. Zhu, and X. Xiao (2005). Mantle structure from inter-station Rayleigh wave dispersion and its tectonic implication in western China and neighboring regions, *Phys. Earth Planet. In.* **148**, no. 1, 39–54, doi: [10.1016/j.pepi.2004.08.006](https://doi.org/10.1016/j.pepi.2004.08.006).
- Zhu, L., and H. Kanamori (2000). Moho depth variation in southern California from teleseismic receiver functions, *J. Geophys. Res.* **105**, no. B2, 2969–2980, doi: [10.1029/1999JB900322](https://doi.org/10.1029/1999JB900322).

Manuscript received 21 October 2021

Published online 4 April 2022